Spatiotemporal quasisolitons and resonant radiation in arrays of silicon-on-insulator photonic wires

C. J. Benton, A. V. Gorbach, and D. V. Skryabin
Centre for Photonics and Photonic Materials, Department of Physics, University of Bath, Bath BA2 7AY, United Kingdom
(Received 25 June 2008; published 12 September 2008)

We have analyzed the conditions for low-power spatiotemporal soliton formation in arrays of evanescently coupled silicon-on-insulator photonic wires. We have verified that pronounced soliton effects can be observed in the presence of realistic loss, two-photon absorption, and higher-order dispersions. A soliton in an N-wire array can excite N resonant frequencies, but some of these may be suppressed due to the soliton having zero projection onto the corresponding radiation supermodes. This results in pronounced differences between the radiation spectra observed from solitons excited at the edge and in the center of arrays.

DOI: 10.1103/PhysRevA.78.033818 PACS number(s): 42.65.Tg, 42.65.Wi, 42.70.Nq, 42.82.Et

I. INTRODUCTION

Ultrafast nonlinear photonics in structured materials is currently a topic of intense research. Over the past few years, the well-established technology of silicon-on-insulator (SOI) has been recognized as being of great value in this field [1–5]. In particular, nanosized silicon waveguides (or photonic wires) and resonators offer extremely promising ways of realizing photonic components on a microchip. This is due to their strong optical confinement and their transparency at the common telecommunications wavelengths near to 1.5 μm. Their substantial (and ultrafast) Kerr nonlinearity [6,7] and strong dispersion (which can be tightly controlled by altering the geometry) [8,9] are important properties in the development of all-optical signal processing devices [10,11].

SOI technology also offers an exciting opportunity to bridge applied and fundamental research, particularly in the area of soliton physics [12–15]. One of the key features of SOI waveguides is that strong anomalous group velocity dispersion (GVD) can be achieved with nanoscaled transverse dimensions. The enhanced nonlinear response resulting from this tight confinement leads to soliton peak powers of only a few watts [12,13,15] (for 100-fs pulses), which is record-breakingly small in optics. The nonlinear effects in SOI wires may be impeded by two-photon absorption (TPA), but this does not preclude the observation of pronounced soliton effects [12–14,16].

One of the central concepts in the area of optical solitons is the spatiotemporal soliton [17,18], whereby light is simultaneously self-localized in time *and* in some or all spatial dimensions. The main difficulties encountered in this field [19–21] arise from the need to provide sufficiently strong anomalous dispersion, sufficient nonlinearity to reduce power requirements to practical levels, and close matching between the dispersion and diffraction lengths.

Confining light into waveguides, but still allowing for coupling between them has a number of advantages for the observation of spatiotemporal solitons. First, it reduces the required power, and second, it allows for tight control of both the diffraction and the dispersion. This idea has been proposed theoretically in the context of multicore fibers [22,23], while recent advances in the fabrication of such fibers have shown great promise for experimental realization [25]. One-dimensional waveguide arrays have also been tried in spatiotemporal nonlinear experiments. The most successful of these have reported spatiotemporal X waves in AlGaAs waveguides [26] and of spatiotemporal focusing in silica waveguides [27].

In this paper, we examine the suitability of arrays of SOI photonic wires for the observation of discrete spatiotemporal solitons. We demonstrate that a suitable design of wires can provide dispersion lengths (for ~100-fs pulses) in the range of 1 mm and coupling lengths of a few millimeters. This appears to be optimal for the creation of solitons with peak powers of the order of a few watts. Despite the destructive influence of TPA, we numerically demonstrate that pronounced soliton effects occur under realistic experimental conditions.

Furthermore, in order to explain peculiar spectral signatures seen in our numerical results, we develop a theory of radiation emission from the spatiotemporal solitons in SOI wire arrays. This describes an effect whereby certain radiation peaks are suppressed for symmetry reasons, resulting from the interplay between spatial and temporal degrees of freedom. This part of our work overlaps with recent reports of supercontinuum and Cherenkov radiation in single SOI wires [14,15] and with the recently published numerical study of temporal modulational instabilities [28] and supercontinuum generation in waveguide arrays [29]. (The latter work, however, does not contain analytical predictions of the frequencies of supercontinuum radiation going beyond the single-waveguide case.)

II. NUMERICAL MODEL AND LINEAR PROPERTIES OF THE PHOTONIC WIRES

Spatiotemporal evolution of light in a waveguide array can be described by dimensionless coupled nonlinear Schrödinger equations (see, e.g., [22,23]) of the form

$$\frac{\partial E_n}{\partial \zeta} - i\hat{D}E_n = i|E_n|^2E_n + i\hat{C}(E_{n-1} + E_{n+1}) - \epsilon_{\mathrm{tpa}}|E_n|^2E_n - \epsilon_1 E_n,$$

$$n = 1,2,\ldots,N, \qquad (1)$$

where E_n is the scalar amplitude of the waveguide mode of a single wire (see Fig. 1). We consider below the mode having

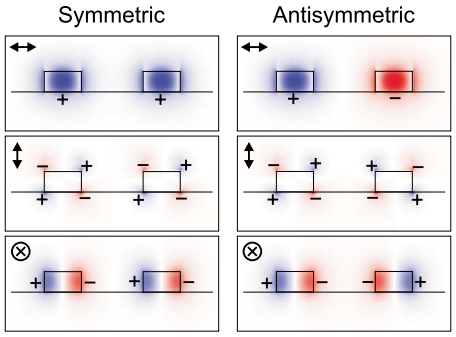

FIG. 1. (Color online) Symmetric (left) and antisymmetric (right) mode profiles, displayed over a 2.4 μm$\times$1 μm cross section. Silica is beneath the horizontal line, with the rectangles denoting the silicon. The electric field vector is split into Cartesian components, with transverse components parallel to the silica-air interface shown top, transverse perpendicular components shown middle, and longitudinal components shown bottom. Color saturation gives the absolute value. The + and − signs (and blue and red regions where color is provided) denote the relative phase. (For clarity, the saturation of the middle figure has been doubled.)

the dominant polarization component parallel to the substrate (TE mode) and neglect possible nonlinear coupling to the modes having the dominant component perpendicular to the substrate (TM mode). This is justified since the effective index of the neglected mode is much smaller and hence the nonlinear coupling into it can be neglected. Also, TM modes are less well confined and suffer from higher losses.

The above model describes only the first transmission band of the waveguide array and disregards the higher-order ones. This is sufficient for our purposes, since we focus below on solitons in the semi-infinite low-lying band gap only, which is practically unaffected by the presence of higher-order bands. The complete band-gap structure and its interplay with the dispersion in two-dimensional liquid infiltrated waveguide arrays have been recently discussed in [24].

Time τ [see Eqs. (2) and (3)] in the frame moving with the group velocity of light at the pump frequency is measured in units of $T_0 \equiv \tau_0/[2\ln(1+\sqrt{2})]$, where τ_0 is the full width at half maximum (FWHM) of the input pulse. In this formulation an input condition of the form $E_n = \mathrm{sech}(\tau)$ corresponds to a physical pulse duration of τ_0. The propagation distance ζ is given in units of the dispersion length $L_\mathrm{D} \equiv T_0^2/|\beta_2|$, where β_2 is the GVD at the pump frequency.

The amplitudes have been scaled such that $P_0|E_n|^2$ gives physical power. The intrinsic unit of power, P_0, is given by $P_0 \equiv 1/\gamma L_\mathrm{D}$, where γ is the nonlinear coefficient. This can be calculated using $\gamma = 2\pi n_2/S\lambda_0$ [30]. For the waveguides studied below (approximately 500 nm$\times$200 nm) the effective area S is of the order 10^{-13} m^2. This method for calculating γ (which is straightforward in optical fibers) is problematic for SOI photonic wires. One reason for this is that the mode profiles of nanosized silicon waveguides have sharp variations at the interfaces (see Fig. 1), which may invalidate the textbook approach. Furthermore, the values for n_2 reported in the literature vary between $\sim 10^{-18}$ and $\sim 10^{-17}$ m^2 W^{-1} [6,7]. A pump wavelength of $\lambda_0 = 1.5$ μm gives values of γ ranging from 40 to 400 W^{-1} m^{-1}, yielding approximate values of P_0 (for $L_D \sim 1$ mm) ranging from 2.5 to 25 W. The comparison of numerical and experimental measurements [12] has yielded values of P_0 close to or less than 1 W. However, the precise value of P_0 is not particularly important for our theoretical studies, as it merely corresponds to a scaling of the input power.

The dispersion operator $\hat{D}$ and coupling operator $\hat{C}$ are defined as

$$\hat{D} = \sum_{m=2}^{M} d_m \left(i \frac{\partial}{\partial \tau} \right)^m, \tag{2}$$

$$\hat{C} = \sum_{m=0}^{M} c_m \left(i \frac{\partial}{\partial \tau} \right)^m, \tag{3}$$

where $d_m \equiv \beta_m L_\mathrm{D}/(m!)T_0^m$ and $c_m \equiv \delta_m L_\mathrm{D}/(m!)T_0^m$. Here β_m are the dispersion coefficients at the 1.5-μm pump wavelength, which were derived from the mode propagation constants at various frequencies. These were calculated directly from Maxwell's equations using the FEMSIM module of the RSOFT software package [31]. The material dispersion of both silicon and silica was accounted for, using the Sellmeier equations given in [32,33]. The operator $\hat{C}$ accounts for coupling and its dispersion. The coefficients $\delta_m \equiv \frac{1}{2}(\beta_{sm} - \beta_{am})$, where β_{sm} and β_{am} are the propagation constants of the symmetric and antisymmetric two-wire supermodes. A polynomial up to $M = 11$ yielded relative fitting errors of the order 10^{-5}. Figure 1 shows the symmetric and antisymmetric supermodes of the two-wire structure used to calculate δ_m.

We assumed a geometry consisting of a silicon wire with rectangular cross section, sitting on top of a slab of silica (and otherwise surrounded by air). We fixed the height of the silicon layer at 220 nm and also assumed the presence of a 100-nm-high etching mask with a refractive index of 1.35. Varying the silicon width, we settled upon values of 380 and 420 nm. Both of these geometries were chosen to give very high (absolute values of) GVD at 1.5 μm (−5400 and −4700 fs^2 mm^{-1}, respectively). The corresponding values of L_D are 0.59 and 0.69 mm for 100-fs FWHM pulses. This is necessary in order to fit a reasonable number of L_D into a realistic waveguide length of 0.5–1 cm, so that we can claim nonlinear suppression of the pulse dispersion. Additionally (as is shown in Sec. III) the GVD imposes an upper bound on the temporal duration of the soliton, and so for low values the necessary input pulses become impractically short. Figure 2 shows the wavelength dependence of $1/L_\mathrm{D}$ for the two geometries. (The dispersion coefficients are given in the caption to this figure.) An important aspect of the 380-nm wire is that it has a zero GVD point at 1.628 μm, which is near to the pump wavelength. Therefore the spectrum of sufficiently short solitons will significantly overlap with the normal GVD range, allowing for Čerenkov radiation [34,35]. (This is studied in detail in Sec. V.) By comparison, the GVD of the 420-nm wire is much further away at 1.735 μm, yielding negligible Čerenkov effects.

We define the pump-wavelength coupling length to be $L_\mathrm{C} \equiv \pi/|\beta_{s0} - \beta_{a0}|$, which is the distance taken for light in a pair of coupled wires to completely transfer from one wire to

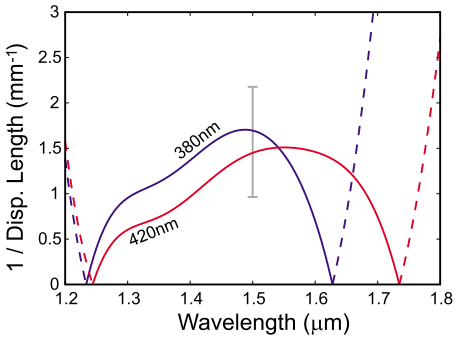

FIG. 2. (Color online) $1/L_D(\lambda)$ for the two waveguide widths. Anomalous (normal) dispersion is represented by solid (dashed) lines. The vertical bar highlights the 1.5-μm pump wavelength. The leading (scaled) dispersion coefficients are $d_2=-0.5$, $d_3=-0.00326$, $d_4=0.00148$, and $d_5=-6.16\times10^{-5}$ for the 380-nm-wide wire and $d_2=-0.5$, $d_3=0.00615$, $d_4=7.00\times10^{-4}$, and $d_5=-4.06\times10^{-6}$ for the 420-nm-wide wire.

the other. Coupling is strongly dependent on wavelength, as is shown in Fig. 3, and can be controlled by altering the distance between neighboring wires. There are two opposing constraints imposed on the L_C. The first is that to study spatial localization we need to have a sufficiently short coupling length. The second is that the choice of L_C is bounded from below by the existence and stability conditions for spatiotemporal solitons, which are discussed in Sec. III. The wire separation we have chosen is 700 nm, which gives $L_C=2.8$ mm for the 380-nm-wide wire and $L_C=3.2$ mm for the 420-nm wire. (The coupling coefficients are given in the caption to Fig. 3.)

The linear absorption and TPA coefficients are ϵ_l and ϵ_{tpa}, respectively. The former is assumed to have a value of 0.01, which corresponds to absorption lengths (defined as the distance taken for intensity to half) of 20 and 24 mm ($\sim$−1.5 dB/cm) in the 380- and 420-nm wires. ϵ_{tpa} is taken to be 0.1 [12,13]. This amounts to replacing the nonlinear index n_2 with $n_2(1+i\epsilon_{tpa})$. The comparison of numerical and experimental results [12] strongly suggests that free-carrier-induced absorption and refractive index change can be neglected for the relatively low powers considered. It should also be mentioned that we assume a pulse repetition time

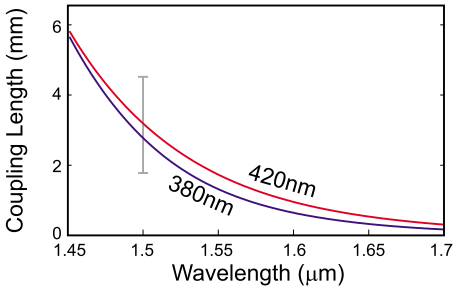

FIG. 3. (Color online) $L_C(\lambda)$ for the two waveguide widths. The vertical bar highlights the 1.5-μm pump wavelength. The leading (scaled) coupling coefficients are $c_0=0.336$, $c_1=-0.106$, $c_2=0.0187$, and $c_3=-0.00213$ for the 380-nm-wide wire and $c_0=0.337$, $c_1=-0.0868$, $c_2=0.0124$, and $c_3=-0.00129$ for the 420-nm-wide wire.

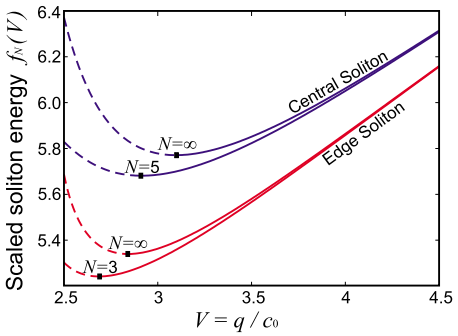

FIG. 4. (Color online) Normalized energy of edge and central solitons $f_N=U/\sqrt{c_0}$, as a function of $V=q/c_0$ shown with $N=\infty$ for both types of solitons and with $N=3$ and $N=5$ for edge and central solitons, respectively. The unstable ($\partial U/\partial q<0$) solitons are denoted by dashed lines. The energy unit P_0T_0 is typically in the vicinity of 100–1000 fJ.

greater than the carrier lifetime ($\sim$10 ns [12]), so the carrier density cannot build up over successive pulses. The influence of the silicon Raman scattering on the short pulses can also be safely neglected [36].

III. SPATIOTEMPORAL SOLITONS

Ideal spatiotemporal solitons are assumed to take the form $E_n(\zeta,\tau)=F_n(\tau)e^{iq\zeta}$. To find the real functions F_n we neglected linear loss, TPA, higher-order dispersion ($d_{m>2}=0$), and coupling dispersion ($c_{m>1}=0$). This gives a set of N ordinary differential equations:

$$\frac{1}{2}\frac{d^2F_n}{d\tau^2} = qF_n - |F_n|^2F_n - c_0(F_{n-1}+F_{n+1}),$$

$$n = 1,2,\ldots,N. \tag{4}$$

Spatiotemporal soliton solutions were then found using a finite-difference Newton-Raphson method. Solitons in Eqs. (4) have been previously reported in the case where edge effects are not important in, e.g., [23]. Edge solitons (i.e., those with a peak amplitude in the $n=1$ wire) have attracted significant recent attention (see, e.g., [37,38]). In what follows we will also consider solitons in the geometries with a small number of wires when edge effects on both ends are important.

In Fig. 4 we plot the soliton energy U, defined as $U\equiv\Sigma_{n=1}^{N}\int_{-\infty}^{\infty}|F_n|^2d\tau$ as a function of the scaled wave number q/c_0. Transforming Eqs. (4) using $F_n'(\tau)\equiv\sqrt{2q}F_n(\sqrt{2q}\tau)$ we obtain

$$\frac{d^2F_n'}{d\tau^2} = F_n' - 2|F_n'|^2F_n' - \frac{1}{V}(F_{n-1}'+F_{n+1}'), \tag{5}$$

where the parameter V is given by $V\equiv q/c_0$. This is useful, as the numerical solution of Eqs. (5) needs only one free parameter (namely, V). One can show analytically that the solitons, stable or unstable, exist within the interval $V\in(V_{ex},\infty)$, where $V_{ex}=2\cos[\pi/(N+1)]$. [See Eq. (13) in Sec. V.] The soliton energy is then $U=\sqrt{c_0}f_N(V)$, where f_N is

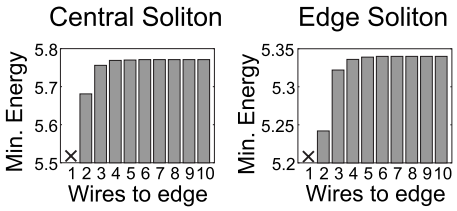

FIG. 5. Effect of the array edges on the minimum soliton energy. To compare the cases of the central and edge solitons, the quantities are plotted against the number of wires separating the pump channel from each edge of the array for the central soliton case and from the far edge of the array for the edge soliton case. The energy unit P_0T_0 is typically in the vicinity of 100–1000 fJ.

derived from the solution to Eq. (5) as $f_N(V) = \sqrt{2V}\Sigma_{n=1}^{N}\int_{-\infty}^{\infty}|F_n'|^2 d\tau$. The function f_N differs between central and edge solitons, with the values being smaller for the latter. In the central and edge cases, the energy $U(V)$ has a minimum at $V=V_{\rm vk}$, $U \geqslant U(V_{\rm vk})$. This energy threshold is slightly lower for an edge soliton. Solitons become unstable for $\partial U/\partial q < 0$ (the Vakhitov-Kolokolov criterion [39,40]), and so for stable soliton propagation it is required that $V \geqslant V_{\rm vk}$.

In Fig. 5 we show how the edge effects affect the lower bound of the soliton energy (at given c_0). The minimum soliton energy is reduced for a restricted number of wires, as the light cannot diffract beyond the edge of the system. In order to meaningfully compare central and edge solitons, we define ΔN as the number of wires separating the maximum intensity wire from the edge. This is given by $N-1$ for an edge soliton and $(N-1)/2$ for a central soliton (in a system with odd N). The edge effects rapidly diminish as ΔN is increased, with the quasi-infinite regime being effectively reached at $\Delta N=5$ or 6. In the case of $\Delta N=1$ (corresponding to $N=2$ for the edge soliton and $N=3$ for the central soliton) it is difficult to determine the locations of the $V=V_{\rm vk}$ points. This is because the computations have to be performed near to the fundamental cutoff points at $V=V_{\rm ex}$, leading to numerical instability. Therefore the $\Delta N=1$ cases in Figs. 5 and 6 are shown with crosses.

The FWHM duration of a soliton, T_s, decreases monotonically with increasing V. An upper bound of T_s can be derived by measuring the soliton duration at $V=V_{\rm vk}$. Scaling back to physical units we find

$$T_s \leqslant \alpha_{\max}\sqrt{2|\beta_2|L_C}, \tag{6}$$

where β_2 is the GVD and L_C is the coupling length at the pump wavelength. This is approximately 80 fs for our chosen geometries. The numerically derived dimensionless number $\alpha_{\max}$ depends on the number of wires and the soliton type. Restricting the number of wires causes a slight upwards correction to $\alpha_{\max}$, as is shown in Fig. 6. Again, this is due to diffraction being constrained by the boundaries.

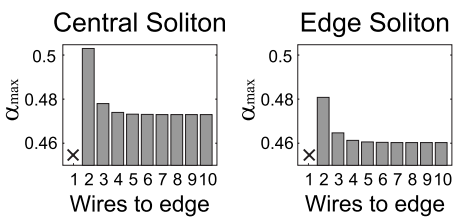

FIG. 6. Parameter $\alpha_{\max}$ (defining maximum soliton duration) as a function of the number of wires between the maximum intensity wire and the array boundary as in Fig. 5.

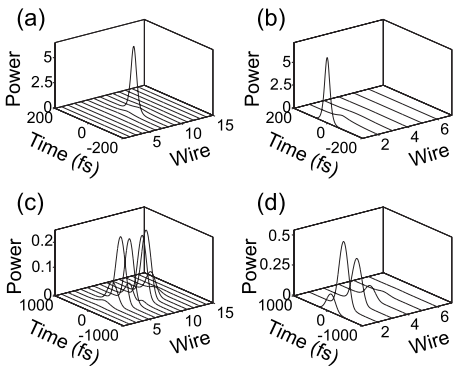

FIG. 7. Evolution of a sech-like pulse (with power $3.5P_0$) sent into a single wire. Center (a) and edge (b) wire excitation results in soliton formation. When nonlinearity is turned off (c) and (d), the pulses disperse and diffract. Power axis is in units of P_0. Propagation distance is 2.7 mm. The model does not include linear loss or TPA.

IV. FORMATION AND DYNAMICS OF SPATIOTEMPORAL QUASISOLITONS

In a real system, losses and higher-order dispersions prevent the formation of idealized unchanging soliton solutions. Therefore, it is more meaningful to speak about the formation of quasisolitons. In order to study quasisoliton formation and evolution, we performed direct numerical modeling of Eqs. (1) using a split-step Fourier method.

As a first step, we will consider the undamped system. This is because the effect of damping is inherently destructive, and so by removing it we can examine quasisoliton evolution more effectively. The central-soliton and edge-soliton solutions described in Sec. III propagate robustly through this system, indicating that long-lasting quasisolitons can exist. [Furthermore, this demonstrates that the assumption of second-order dispersion and fixed coupling in Eq. (4) is appropriate.]

Firing a preformed soliton into an array of wires is impractical in a real-life experiment. Therefore, any realistic modeling must be based upon the injection of a single pulse [in this case, of the form $E \propto \mathrm{sech}(\tau)$] into a single wire. Central and edge quasisolitons can indeed be created like this, as is shown in Fig. 7. (Pulses with a 100-fs duration and a peak power of $3.5P_0$ were used, and damping is still absent.)

We should also note that the chosen 100-fs pulse duration is longer than the ≈80-fs upper bound to soliton duration given by Eq. (6). However, soliton formation still occurs due to the so-called soliton compression effect (see, e.g., [30,41]), which occurs during the initial stages of pulse evolution. This process is demonstrated in Fig. 8, where linear losses and TPA have been reintroduced to the model. This

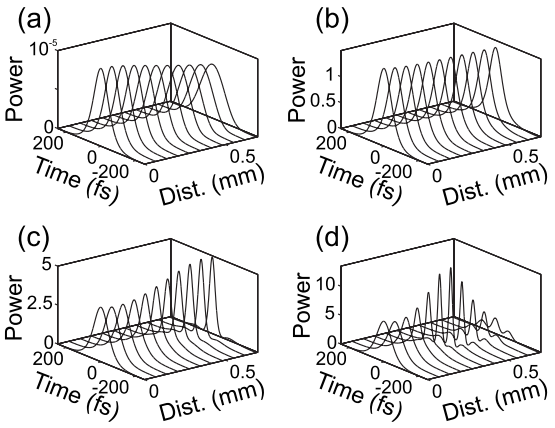

FIG. 8. 100-fs pulse evolution in a 420-nm-wide wire over one dispersion length (0.69 mm). At very low power (a) the pulse broadens. At $1.5P_0$ (b) a quasisoliton (with an approximate duration of 100 fs) is formed. At $3.5P_0$ (c), the pulse is compressed to 34 fs. Increasing the power to $7P_0$ (d) results in pulse splitting (soliton fission). Power axis is in units of P_0. The model includes linear loss and TPA.

shows that a 100-fs pulse (with power $3.5P_0$) is compressed to 34 fs after only 0.7-mm propagation. This propagation distance is much less then the coupling length (~3 mm), and so the coupling into neighboring wires is not important. It can also be seen that the $3.5P_0$ power is roughly optimal, as increasing it further causes multisoliton fission.

Figures 9 and 10 demonstrate quasisoliton formation when all absorption terms are present. Localization in both space and time is established over a distance of the order of the coupling length. Although the localization becomes less pronounced with further propagation, it is clear that the correct choice of wire length (for the given input power and coupling) leads to pronounced nonlinear switching, which is accompanied by the formation of a spatiotemporal quasisoliton.

V. RESONANT RADIATION OF SPATIOTEMPORAL SOLITONS

As has been mentioned above, the overlap of the soliton spectrum with the normal GVD region should lead to the

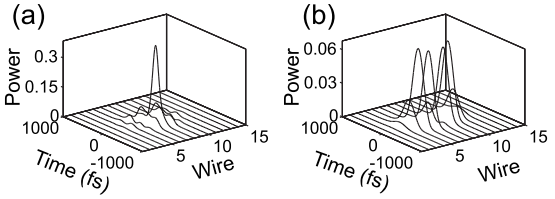

FIG. 9. Result of a 100-fs pulse with peak power $3.5P_0$ being fired into the central wire ($n=8$) of a 15-wire array (of 220 nm $\times$420 nm wires placed 700 nm apart). Propagation distance is 2.7 mm. With nonlinearity (a) the light is localized in the input wire, and broadening in time and space is suppressed, indicating quasisoliton formation. When nonlinerity is turned off (b) diffraction has transferred nearly all the light from the pump wire into nearest and next-nearest neighbors. Power axis is in units of P_0. The model includes linear losses and TPA.

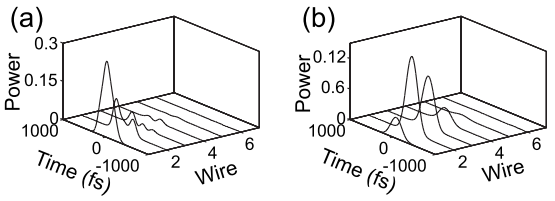

FIG. 10. The same as Fig. 9, but with the pulse fired into the edge wire ($n=1$) of a 15-wire array. (a) shows the quasisoliton formation for $3.5P_0$ input power, and (b) shows linear diffraction. The model includes linear losses and TPA. Wires 8–15 (which contain almost no light) are omitted for clarity.

emission of resonant Čerenkov radiation. In this section, we extend the theoretical analysis for a single waveguide [34,42] to an array of waveguides. Defining $\epsilon_n(\zeta,\tau)$ to be a linear perturbation which propagates on the soliton background, we substitute

$$E_n(\zeta,\tau) = [F_n(\tau) + \epsilon_n(\zeta,\tau)]e^{iq\zeta} \tag{7}$$

into Eqs. (1) to give

$$iq\epsilon_n + \frac{\partial \epsilon_n}{\partial \zeta} = (2\epsilon_n + \epsilon_n^*)F_n^2 + i\hat{D}\epsilon_n + i\hat{C}(\epsilon_{n+1} + \epsilon_{n-1}) + i\left[\hat{D} - \frac{1}{2}\frac{\partial^2}{\partial \tau^2}\right]F_n + i[\hat{C} - c_0](F_{n+1} + F_{n-1}), \tag{8}$$

where the terms containing ϵ^2 and ϵ^3 have been discounted. The resonances of the above system with the linear unbound waves

$$\epsilon_n = \epsilon_n' e^{ik_z\zeta - i\omega\tau} \tag{9}$$

can be found when the driving terms (i.e., those containing F_n but not ϵ_n) are removed. We also neglect the $(2\epsilon_n + \epsilon_n^*)F_n^2$ term (which describes the local refractive index change induced by the soliton field). While this term is of importance when calculating the radiation amplitude [42], it can be neglected when we merely wish to determine the frequency of the resonance. The resonance condition is $k_z = 0$, which corresponds to the wave numbers of a soliton and a linear wave being matched. The resulting system of equations is

$$\left(\frac{q - D(\omega)}{C(\omega)}\right)\epsilon_n' = \epsilon_{n+1}' + \epsilon_{n-1}', \quad n = 1,2,\ldots,N. \tag{10}$$

The above system can be interpreted as an eigenvalue problem with the coefficient on the left-hand side being an eigenvalue. It is relatively straightforward to demonstrate that nontrivial solutions for ϵ_n' exist providing that

$$q = D(\omega_j) + 2C(\omega_j)\cos\left(\frac{j\pi}{N+1}\right), \quad j = 1,2,\ldots,N, \tag{11}$$

where the index j labels the different modes and their resonant frequencies. The cosine function on the right-hand side has unique values for all j, as its argument does not go outside of the $(0,\pi)$ interval. This implies that N distinct reso-

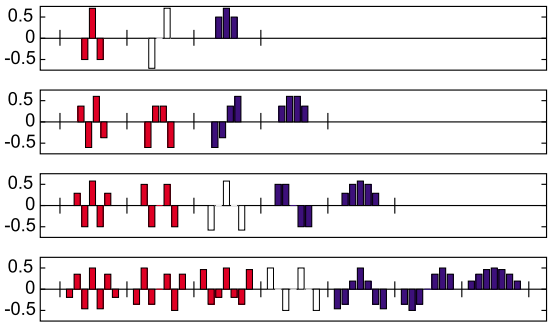

FIG. 11. (Color online) Normalized eigenvectors for Eq. (10). Shown for (top to bottom) $N=3$, 4, 5, and 7. The eigenvectors are arranged by order of their corresponding eigenvalue, which increases from left to right. Modes with negative eigenvalues are shown in red (dark gray), while modes with positive eigenvalues are shown in blue (light gray).

nant frequencies will exist. It follows from the identity $\cos(\theta) \equiv -\cos(\pi - \theta)$, that the values of the cosine function occur in pairs having opposite signs.

The corresponding (normalized) eigenvectors are

$$\epsilon'_{nj} = \sqrt{\frac{2}{N+1}} \sin\left(\frac{nj\pi}{N+1}\right). \tag{12}$$

The eigenvectors for a selection of N values are shown in Fig. 11. If N is odd, then $j=(N+1)/2$ implies the resonance condition $q-D(\omega_j)=0$, which is identical to the one found in an isolated waveguide. The corresponding eigenvector is such that the waveguides with the nonzero radiation intensities are separated by the ones where radiation is completely absent. Applying the transformation $\epsilon'_n \to (-1)^n \epsilon'_n$ to any eigenvector will yield the eigenvector with oppositely signed eigenvalue. Therefore, the modes exist in matched pairs having the same power distribution between the wires, but opposing interwire phase relationships.

Furthermore, the eigenvectors can be divided into symmetric and antisymmetric types (with respect to reversing the ordering of the wires). By antisymmetric we mean that the fields in the wires equidistant from the center of an array have the same magnitudes, but are π out of phase. There are always $\lceil N/2 \rceil$ symmetric modes and $\lfloor N/2 \rfloor$ antisymmetric modes (where $\lceil x \rceil$ means round x up to the nearest integer and $\lfloor x \rfloor$ means round down).

The absence of a resonance at $\omega=0$ [where $D(0)=0$ and $C(0)=c_0$] defines the fundamental soliton existence condition

$$V > 2\cos\left(\frac{\pi}{N+1}\right) \equiv V_{\mathrm{ex}}, \tag{13}$$

where (as before) $V \equiv q/c_0$. The lower bound of $V=V_{\mathrm{ex}}$ increases with N and tends towards 2 as N goes to infinity.

Graphical solutions of the resonance conditions given by Eq. (11) are shown in Fig. 12. The straight horizontal lines correspond to the left-hand side of (11) and the curved lines to its right-hand side. One can see that the number of resonances coincides with the number of wires, N, and that as N increases the resonance frequencies start to form a continuous band. In the limit of a soliton in an infinite array, the radiation spectrum becomes a continuum, which is bounded on both sides. In this limit, the solutions in Eq. (9) can be replaced with $\epsilon_n = \epsilon e^{ik_z\zeta - i\omega t + i\kappa n}$, where κ is a continuously varying quasimomentum. The corresponding resonance condition is

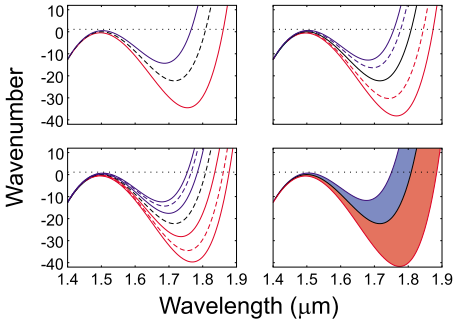

FIG. 12. (Color online) Resonance conditions for 220 nm $\times$ 380 nm wires placed 700 nm apart for systems with (top, left) 3, (top, right) 5, (bottom, left) 7, and (bottom, right) ∞ wires. The soliton wave number $q=1.1$ is given by the horizontal dotted line. Antisymmetric modes are shown as dashed and symmetric modes as solid lines. Modes with negative eigenvalues are shown in red (dark gray) and those with positive eigenvalues in blue (light gray).

$$q = D(\omega) + 2C(\omega)\cos(\kappa). \tag{14}$$

An interesting observation is that in the case when the pump pulse is sent into a central waveguide of an array with a small number of wires, we do not observe the spectral peaks corresponding to antisymmetric radiation modes.

In this situation, it follows that $F_n = F_{\tilde{n}}$ and $\epsilon_n = -\epsilon_{\tilde{n}}$, where the reversed-order wire index $\tilde{n}$ is defined as $\tilde{n} \equiv N+1-n$. Substituting these into Eq. (8) gives

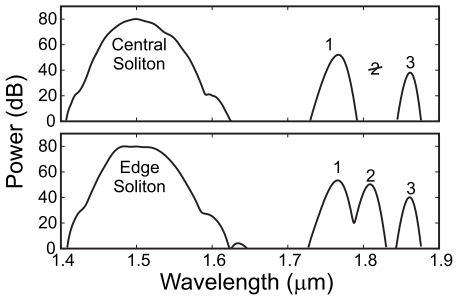

FIG. 13. Power spectrum summed over all wires (after 2.4-mm propagation, $\zeta=4$) for $N=3$ array of 220 nm $\times$ 380 nm wires with 700 nm separation. Shown for center-wire input (top) and edge-wire input (bottom). As predicted, all three Čerenkov peaks are present for the edge soliton, but one of these is suppressed for the central soliton. The input pulse is taken as $\sqrt{3.5P_0}\mathrm{sech}(\tau)$.

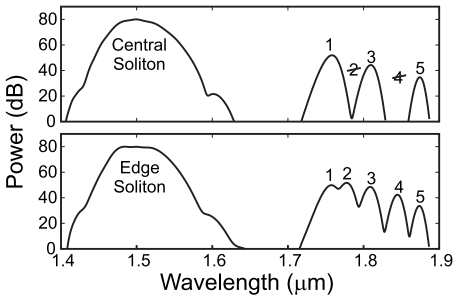

FIG. 14. The same as Fig. 13, but for $N=5$. All five Čerenkov peaks are present for the edge soliton, but two of them are suppressed for the central soliton.

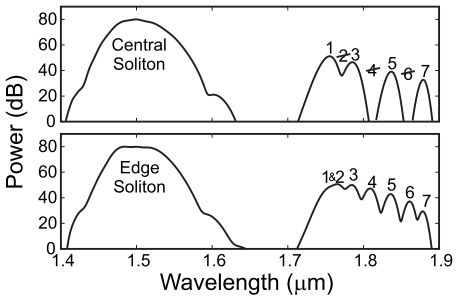

FIG. 15. The same as Figs. 13 and 14, but for $N=7$. All seven Čerenkov peaks are present for the edge soliton, but three of them are suppressed for the central soliton. Peaks 1 and 2 cannot be resolved here, but by observing the modal profiles it can be shown that two resonances are indeed present.

$$iq\epsilon_{\tilde{n}} + \frac{\partial \epsilon_{\tilde{n}}}{\partial \zeta} = (2\epsilon_{\tilde{n}} + \epsilon_{\tilde{n}}^*)F_{\tilde{n}}^2 + i\hat{D}\epsilon_{\tilde{n}} + i\hat{C}(\epsilon_{\tilde{n}+1} + \epsilon_{\tilde{n}-1}) - i\left[\hat{D} - \frac{1}{2}\frac{\partial^2}{\partial \tau^2}\right]F_{\tilde{n}} - i[\hat{C} - c_0](F_{\tilde{n}+1} + F_{\tilde{n}-1}). \tag{15}$$

Dropping the $\tilde{n}$ notation in Eqs. (15) and adding them to Eqs. (8) gives

$$iq\epsilon_n + \frac{\partial \epsilon_n}{\partial \zeta} = (2\epsilon_n + \epsilon_n^*)F_n^2 + i\hat{D}\epsilon_n + i\hat{C}(\epsilon_{n-1} + \epsilon_{n+1}). \tag{16}$$

This lacks any form of driving term, and so for an initial condition of $\epsilon_n=0$, the solution will remain at $\epsilon_n=0$. Therefore, a symmetrical soliton will not radiate into the antisymmetric modes. As $\lfloor N/2 \rfloor$ antisymmetric modes are present, we can therefore predict that $\lfloor N/2 \rfloor$ spectral peaks will be "forbidden." For an edge soliton, however, the above argument will no longer hold (due to the $F_n=F_{\tilde{n}}$ predicate being no longer true). Therefore, all of the modes are permitted for edge solitons.

Figures 13–15 show numerical prediction for the results of a real experiment, in which solitons and edge solitons are excited in small waveguide arrays (for $N=3$, 5, and 7) and the Čerenkov radiation observed. Our model includes linear absorption, TPA, higher-order dispersion, and dispersion of coupling. We have assumed a laser setup capable of firing 100-fs transform-limited sech-like pulses into a single wire. In order to demonstrate that forbidden modes are not excited in any of the wires, we have plotted the spectra of the combined output from all the wires. (Experimentally, this corresponds to the output from the entire array being collected and fed into an optical spectrum analyzer.) The resulting spectrum can then be used to gauge the formation of quasisolitons within the array.

VI. CONCLUSIONS

We have proposed and theoretically studied an experimental setup based upon silicon-on-insulator wire arrays, which is capable of demonstrating the formation of spatiotemporal quasisolitons. We have shown analytically and numerically that a soliton in an N-wire system, with a zero GVD point close to the pump wavelength, is capable of exciting N resonant frequencies. However, some of these may be suppressed due to the soliton having zero projection onto the multiwire supermode into which the radiation would be emitted. This is of particular interest in a system with a small number of wires, as the spectral lines can be resolved and thus counted. We have numerically predicted the spectral output of potential experiments with central and edge spatiotemporal solitons and have demonstrated their agreement with our analytical predictions.

[1] P. Dumon, G. Priem, L. R. Nunes, W. Bogaerts, D. Van-Thourhout, P. Bienstman, T. K. Liang, M. Tsuchiya, P. Jaenen, S. Beckx *et al.*, Jpn. J. Appl. Phys., Part 1 **45**, 6589 (2006).
[2] Q. Lin, O. J. Painter, and G. P. Agrawal, Opt. Express **15**, 16604 (2007).
[3] M. A. Foster, A. C. Turner, M. Lipson, and A. L. Gaeta, Opt. Express **16**, 1300 (2008).
[4] M. Lipson, J. Lightwave Technol. **23**, 4222 (2005).
[5] R. Dekker, N. Usechak, M. Frst, and A. Driessen, J. Phys. D **40**, R249 (2008).
[6] A. D. Bristow, N. Rotenberg, and H. M. van Drielb, Appl. Phys. Lett. **90**, 191104 (2007).
[7] Q. Lin, J. Zhang, G. Piredda, R. W. Boyd, P. M. Fauchet, and G. P. Agrawal, Appl. Phys. Lett. **91**, 021111 (2007).
[8] A. C. Turner, C. Manolatou, B. S. Schmidt, M. Lipson, M. A. Foster, J. E. Sharping, and A. L. Gaeta, Opt. Express **14**, 4357 (2006).
[9] E. Dulkeith, F. Xia, L. Schares, W. M. J. Green, and Y. A. Vlasov, Opt. Express **14**, 3853 (2006).
[10] Y. Vlasov, W. M. J. Green, and F. Xia, Nat. Photonics **2**, 242 (2008).
[11] F. N. Xia, L. Sekaric, and Y. Vlasov, Nat. Photonics **1**, 65 (2007).
[12] W. Ding, C. Benton, A. V. Gorbach, W. J. Wadsworth, J. C. Knight, D. V. Skryabin, M. Gnan, M. Sorrel, and R. M. De-La-Rue, Opt. Express **16**, 3310 (2008).

[13] J. Zhang, Q. Lin, G. Piredda, R. W. Boyd, G. P. Agrawal, and P. M. Fauchet, Opt. Express **15**, 7682 (2007).
[14] I.-W. Hsieh, X. Chen, X. Liu, J. I. Dadap, N. C. Panoiu, C.-Y. Chou, F. Xia, W. M. Green, Y. A. Vlasov, and R. M. Osgood, Opt. Express **15**, 15242 (2007).
[15] L. Yin, Q. Lin, and G. P. Agrawal, Opt. Lett. **32**, 391 (2007).
[16] Y. Silberberg, Opt. Lett. **15**, 1005 (1990).
[17] B. A. Malomed, D. Mihalache, F. Wise, and L. Torner, J. Opt. B: Quantum Semiclassical Opt. **7**, R53 (2005).
[18] Y. Silberberg, Opt. Lett. **15**, 1282 (1990).
[19] P. Di Trapani, D. Caironi, G. Valiulis, A. Dubietis, R. Danielius, and A. Piskarskas, Phys. Rev. Lett. **81**, 570 (1998).
[20] P. Di Trapani, G. Valiulis, A. Piskarskas, O. Jedrkiewicz, J. Trull, C. Conti, and S. Trillo, Phys. Rev. Lett. **91**, 093904 (2003).
[21] X. Liu, K. Beckwitt, and F. Wise, Phys. Rev. Lett. **85**, 1871 (2000).
[22] A. B. Aceves, C. D. Angelis, A. M. Rubenchik, and S. K. Turitsyn, Opt. Lett. **19**, 329 (1994).
[23] A. V. Buryak and N. N. Akhmediev, IEEE J. Quantum Electron. **31**, 682 (1995).
[24] P. D. Rasmussen, A. S. Sukhorukov, D. N. Neshev, W. Krolikowski, O. Bang, J. Lsgaard, and Y. S. Kivshar, Opt. Express **16**, 5878 (2008).
[25] U. Ropke, H. Bartelt, S. Unger, K. Schuster, and J. Kobelke, Opt. Express **15**, 6894 (2007).
[26] Y. Lahini, E. Frumker, Y. Silberberg, S. Droulias, K. Hizanidis, R. Morandotti, and D. N. Christodoulides, Phys. Rev. Lett. **98**, 023901 (2007).
[27] D. Cheskis, S. Bar-Ad, R. Morandotti, J. S. Aitchison, H. S. Eisenberg, Y. Silberberg, and D. Ross, Phys. Rev. Lett. **91**, 223901 (2003).
[28] A. V. Yulin, D. V. Skryabin, and A. G. Vladimirov, Opt. Express **14**, 12347 (2006).
[29] I. Babushkin, A. Husakou, J. Herrmann, and Y. S. Kivshar, Opt. Express **15**, 11978 (2007).
[30] G. P. Agrawal, *Nonlinear Fiber Optics* (Academic Press, San Diego, 2001).
[31] RSoft Design Group Inc. (http://www.rsoftdesign.com).
[32] I. H. Malitson, J. Opt. Soc. Am. **55**, 1205 (1965).
[33] D. E. Palik, *Handbook of Optical Constants of Solids* (Academic Press, Boston, 1985).
[34] N. Akhmediev and M. Karlsson, Phys. Rev. A **51**, 2602 (1995).
[35] D. V. Skryabin, F. Luan, J. C. Knight, and P. S. Russell, Science **301**, 1705 (2003).
[36] L. H. Yin, Q. Lin, and G. P. Agrawal, Opt. Lett. **31**, 1295 (2006).
[37] D. Mihalache, D. Mazilu, F. Lederer, and Y. S. Kivshar, Opt. Express **15**, 589 (2007).
[38] D. Mihalache, D. Mazilu, F. Lederer, and Y. S. Kivshar, Opt. Lett. **32**, 2091 (2007).
[39] M. Vakhitov and A. Kolokolov, Radiophys. Quantum Electron. **16**, 783 (1973).
[40] D. Skryabin, Physica D **139**, 186 (2000).
[41] M. Foster, A. Gaeta, Q. Cao, and R. Trebino, Opt. Express **13**, 6848 (2005).
[42] F. Biancalana, D. V. Skryabin, and A. V. Yulin, Phys. Rev. E **70**, 016615 (2004).